Metasurface Optics with on-axis Polarization Control for Terahertz Sensing Applications

Thomas S. Nowack, Yash D. Shah, James P. Grant, Ivonne Escorcia Carranza, Mitchell G. Kenney, Daniele Faccio, Edward Wasige, *Senior Member, IEEE*, and David R. S. Cumming, *Fellow, IEEE*

***Abstract*—Non-destructive testing and imaging of materials with unknown properties are important applications of terahertz technology. Different contrast forming methods are available to obtain diverse information on the imaged region, including intensity, color, phase and polarization. Polarimetric imaging is relatively under-investigated owing to the difficulty in its implementation with complex optical arrangements. In this paper we present the design and monolithic fabrication of an anisotropic metasurface that incorporates several beam forming functions in a single layer with high efficiency thus simplifying instrument construction. The probe beam generated by the metasurface consists of an orthogonally polarized pair of collinear Bessel beams that create a well-defined on-axis change of polarization. The metasurface is integrated into a polarimetric imaging microscope for 3D beam profiling and sensing experiments at 2.52 THz. An analytical model to describe the on-axis polarization variation was found to be in excellent agreement with both finite-difference time-domain (FDTD) simulations and the experimental results. The setup was used to measure the refractive index and diattenuation of homogeneous sample regions in a proof-of-principle application. We anticipate this technology will find future application in non-destructive testing and polarimetric imaging of polymer composites and 3D profilometry of reflective surfaces.**

***Index Terms*— Metasurfaces, Optical polarization, Terahertz wave imaging, Nondestructive testing, Dielectric materials**

I. Introduction

THE terahertz region of the electromagnetic spectrum lies in the wavelength range of 10 µm to 3 mm [1]. Terahertz imaging [2, 3] is a major opportunity for applications such as security [4-6] or bio-medical imaging [7, 8], astronomy [9] and non-destructive testing (NDT) [10-12]. Spectroscopy is also well advanced, offering the potential for spectroscopic imaging [9, 10]. Terahertz radiation is non-ionizing, hence suitable for human body imaging [5, 8], delivers sub-millimeter resolution [10-12] and offers several molecular absorption bands [9]. Furthermore, many industrial materials including polymers [11], cardboard [6] and textiles [4, 5] are relatively transparent at terahertz wavelengths so that obscured objects can be reliably imaged.

Whilst many advances have been made in developing suitable technologies to operate in the terahertz band, there is still considerable need for improvement [1, 13]. Compact high-power sources and sensitive detectors are limiting factors for many applications [3]. Bolometric detection at room temperature is widely used for cameras with large pixel-arrays despite the high thermally-induced noise floor ($E_{ph}(THz) \sim k_b T$) [2]. The performance of terahertz imaging systems is further compromised by losses arising from unwanted reflections [14, 15], atmospheric and material absorption [9, 15] and misalignment between individual optical components. Standing waves between constituent components can further deteriorate the performance as a result of unwanted interference [14]. As a consequence of low power sources, lossy optics and low detection sensitivity, terahertz setups often suffer from a low signal-to-noise ratio (SNR) [7].

One promising strategy to overcome the noise limitation of terahertz systems is to develop efficient and highly integrated optical components that enable construction of compact systems with advanced functions [3, 13]. Metasurface optics can compress several components into a single layer [16-18], eliminating the problems associated with interference occurring between traditional components. Rigorous optimization with FDTD simulations and precise fabrication typically result in high transmission (≥70 %) even for complex optical functions [16-19]. Metasurface optics may therefore simplify construction of imaging systems to improve SNR, unlocking the potential for advanced imaging techniques that would otherwise be unfeasible. It has been previously shown that a metasurface can be designed to analyze the state of polarization (SoP) of terahertz beam [20]. In this work we explore the capability of metasurfaces to manipulate the SoP into complex 3D profiles [16-19, 21, 22] and form a probe beam for sensing applications. The SoP describes the spatio-temporal oscillation of the electric field vector of an electromagnetic wave at a given

Manuscript received December 21, 2022; revised February 20, 2023; accepted February 23, 2023. (*Corresponding author: Thomas S. Nowack).*

This project has received funding from the European Union's Horizon 2020 research and innovation programme under the Marie Skłodowska-Curie grant agreement No. 765426 (TeraApps) and the UK Quantum Technology Hub in Quantum Imaging (EP/T00097X/1).

Thomas S. Nowack, James P. Grant, Ivonne Escorcia, Mitchell Kenney, Edward Wasige and David R. S. Cumming are with the James Watt School of Engineering, University of Glasgow, G128LT Glasgow, United Kingdom (e-mail: thomas.nowack@glasgow.ac.uk).

Yash D. Shah and Daniele Faccio are with the School of Physics and Astronomy, University of Glasgow, G128LT Glasgow, United Kingdom.

Supplemental materials and underlying datasets are available online at http://dx.doi.org/10.5525/gla.researchdata.1407.

Color versions of one or more of the figures in this article are available online at http://dx.doi.org/10.5525/gla.researchdata.1407.

Digital Object Identifier INSERT IEEE DOI HERE.

position. For a wave propagating in z direction, the time-averaged SoP is fully described by the transversal E-field components $\vec{E}_x, \vec{E}_y$ and the phase shift δ between them [23].

A dielectric metasurface typically consists of periodic structures with sub-wavelength dimension in one [24] or more directions [25]. The smallest periodic volume is defined as unit-cell, which includes the sub-wavelength structures – often referred to as meta-atoms – that manipulate the properties of light in a well-defined manner. Every meta-atom across a metasurface can be tailored to manipulate transmission properties with sub-wavelength spatial resolution, including phase and birefringence to impart complex phase and polarization profiles. The ability to impose two independent phase functions on to an orthogonal pair of polarizations (OPP) has been previously demonstrated [16, 17, 19, 21, 22]. Each OPP consists of two SoP situated at antipodal points on the Poincare sphere. The normalized Stokes parameters ($S_0 \equiv 1$) form a Cartesian coordinate system on the Poincare sphere, with $S_1 = +(-)\,1$ referring to horizontally (vertically) polarized light, $|H\rangle$ ($|V\rangle$), $S_2 = +(-)\,1$ describing (anti-)diagonally polarized light, $|D\rangle$ ($|A\rangle$), and $S_3 = +(-)\,1$ describing right (left) circularly polarized light, $|R\rangle$ ($|L\rangle$).

These metasurface capabilities can be exploited to generate new types of beam forming optics based on Bessel beams [19, 21, 26]. Bessel beams exhibit a transversal intensity profile that follows a Bessel function of nth order, which is retained along the optical axis in a non-diffracting manner. By introducing independent phase-encoding onto an OPP, a new class of Bessel beam can be generated that changes its SoP along the optical axis [19, 27-29]. A probe beam of this type has great potential as a beam forming optic owing to the beam's ability to retain focus over large axial distances, its self-healing capacity after encountering obstructions [29, 30] and the well-defined correlation between propagation distance z and transversal SoP [28]. A wide range of materials exhibit polarization-dependent properties, such as birefringence or diattenuation, that alter the transmitted SoP profile of such a probe beam. These effects can be used for material identification, characterization and defect analysis [4, 18].

The terahertz probe beam is composed of a collinear pair of orthogonally polarized Bessel beams to generate an extended focal line with linearly varying SoP along the propagation direction. The monolithically etched metasurface compresses the entire beam forming function into a single layer. The measured etch depth tolerance of $\pm$ 2.3 % ($\pm\sigma$) was found to only alter the desired phase shift of each meta-pillar by $\pm$7.1° to $\pm$22.8°. depending on the pillar geometry (W_x, W_y) The new optical component was integrated into a polarimetric terahertz microscope that was used to demonstrate the retrieval of multiple pieces of sample information including the refractive index and diattenuation using a model that accurately described the observed on-axis polarization effects.

II. Design and Methodology

A. Design and Operation of the Metasurface

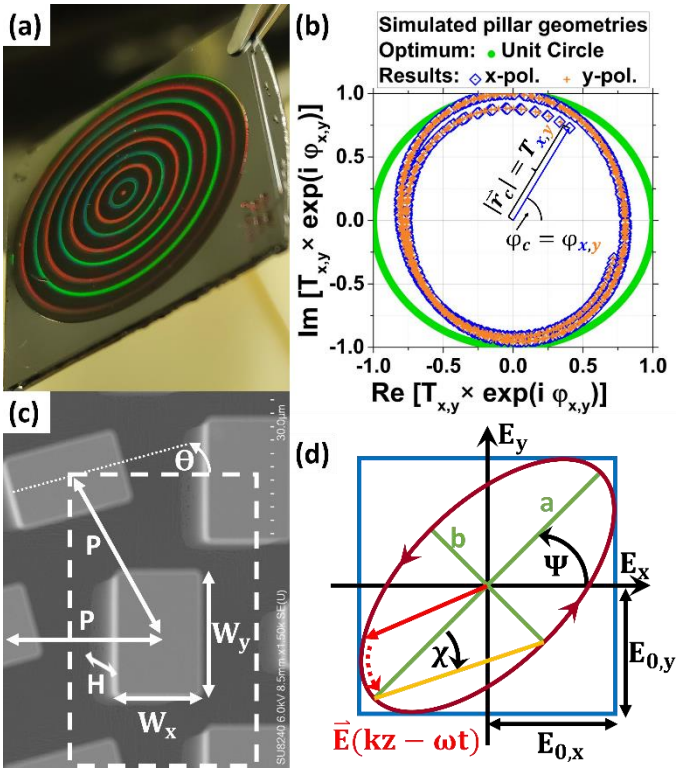

Fig. 1. (a) The fabricated metasurface exhibiting interference colors (radius R_{MS} = 11 mm). (b) Scanning electron micrograph of the metasurface's unit cell (white dashed box). Chosen parameters are pillar height H = 150 µm, nearest neighbor distance P = 40 µm, pillar widths (W_x and W_y) from 15 µm to 30 µm with a 0.5 µm step-size, and the in-plane rotation angle Θ in the range from [0°, 180°] with 1° step-size. (c) Polar plot of the complex transmission for all simulated pillar geometries under incident x- (blue diamonds) and y-polarized light (orange crosses). (d) Illustration of the polarization ellipse (dark red) describing the transverse oscillation of the E-field vector (red arrow), which is fully defined by the orientation and ellipticity angles $\Psi \in [-90°, +90°]$ and $\chi \in [-45°, +45°]$, respectively.

The design of our dielectric metasurfaces is based on rectangular pillars (meta-atoms) with 150 µm pillar height H, whose anisotropic widths $W_x,\ W_y \in [15\,\mu m; 30\,\mu m]$ are optimized together with the in-plane rotation angle $\theta \in [0°; 180°]$ for each lattice point l of a hexagonal lattice with nearest neighbor distance P of 40 µm, following an established routine for polarization-dependent phase encoding [16, 17, 21, 22], as detailed in supplement section S1. Intrinsic silicon (resistivity > 10 kΩcm) was chosen for both the substrate and pillars because of its high refractive index of 3.418 refractive index units (RIU) [31] and transparency at the design wavelength λ_0 of 118.8 µm. Fig. 1 (a) and (b) shows the fabricated metasurface with its optimized unit cell, respectively. The polar plot of Fig. 1 (c) summarizes simulation results of the unit cell for different pillar geometries. Each data point

represents the complex transmission (radial distance $|\vec{r}_c| = T_{x,y}$, polar angle $\varphi_c = \varphi_{x,y}$) of a specific pillar geometry (W_x, W_y) for incident x- and y-polarized light (blue squares and orange crosses, respectively). The imparted phase shifts $\varphi_{x,y}$ span a full phase period of $[-\pi, +\pi]$ while the transmission $T_{x,y}$ remained high and uniform at an average value of 86.9 % ± 6.4 % for both polarizations, close to optimal performance (green circle).

The metasurface was designed to produce an extended focal line in which the SoP changes linearly as a function of the distance along the optical axis z. This was done by encoding two spatial phase functions $\varphi_{1,2}(x_l, y_l)$ that are independently excited by an OPP, in our case by incident $|L\rangle$ or $|R\rangle$ polarized light [27]. All parameters resulting from these two phase functions are subsequently denoted by the subscripts "1" and "2". Both phase functions $\varphi_{1,2}(x_l, y_l)$ were implemented as axicons with different radial phase periods $g_1 < g_2$ according to (1), with the radial distance $|\vec{r}_l|$ to the center of the metasurface and x_l, y_l the Cartesian coordinates of each respective lattice point l.

$$\boldsymbol{\varphi_{1,2}(x_l, y_l) = 2\pi \cdot \underbrace{\sqrt{x_l^2 + y_l^2}}_{:=|\vec{r}_l|} \cdot \frac{1}{g_{1,2}}} \qquad \textbf{(1)}$$

Fig. 2 (a) and (b) show the phase shifts (color code) imparted on incident $|L\rangle$ and $|R\rangle$ polarized light by the selected meta-pillars at each lattice point (black dots) to approximate the phase functions φ_1 and φ_2 with g_1 and g_2 of 0.24 mm and 0.4 mm, respectively. The pattern algorithm (supplement section S1) accurately approximated both orthogonal phase profiles.

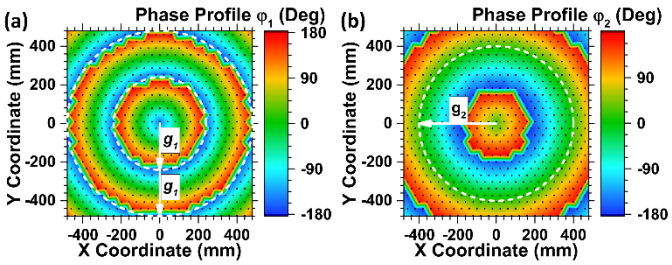

Fig. 2. 2-dimensional x-y phase profiles (axicons) generated by the pattern algorithm of supplement section S1 according to (1) to generate different phase profiles $\varphi_{1,2}$ with (a) radial phase period g_1 of 0.24 mm for incident $|L\rangle$ polarized light and (b) g_2 of 0.4 mm for incident $|R\rangle$ polarized light, respectively. The white arrows and dashed circles indicate the radial phase periods $g_{1,2}$ and the black dots indicate lattice points l at which the optimized meta-pillars were placed.

Collective simulations using the software Lumerical FDTD solutions are shown in Fig. 3 for the metasurface of Fig. 2 with radius R_{MS} of 2 mm (9'061 individual pillars). The x-z intensity profiles (y = 0) in Fig. 3 (a) and (b) confirm that both phase functions φ_1 and φ_2 work independently to generate different Bessel beams, B_1 or B_2, upon excitation by incident $|L\rangle$ or $|R\rangle$ light, respectively. The half-cone angles $\alpha_{1,2} = sin^{-1}(\lambda_0/g_{1,2})$ [27] and non-diffracting focal lengths $z_{max1,2} = R_{MS}/\,tan\,\alpha_{1,2}$ of the two Bessel beams $B_{1,2}$ are illustrated in Fig. 3 (a) and (b) as white dashed lines that accurately describe the simulation results. The black dashed lines describe the transverse diameter of the focal line $d_{f1,2} = 2.405 \cdot \lambda_0/(\pi\, sin(\alpha_{1,2}))$, with $d_{f1} < d_{f2}$ [30]. The transverse circular area (square area for simulations) around the optical axis spanned by the diameter $2/3 \cdot d_{f1}$ will henceforth be used to define the SoP at the beam center for any given on-axis position z. The SoP along the focal line remained circularly polarized with inverted handedness for both individual beams of Fig. 3 (a) and (b).

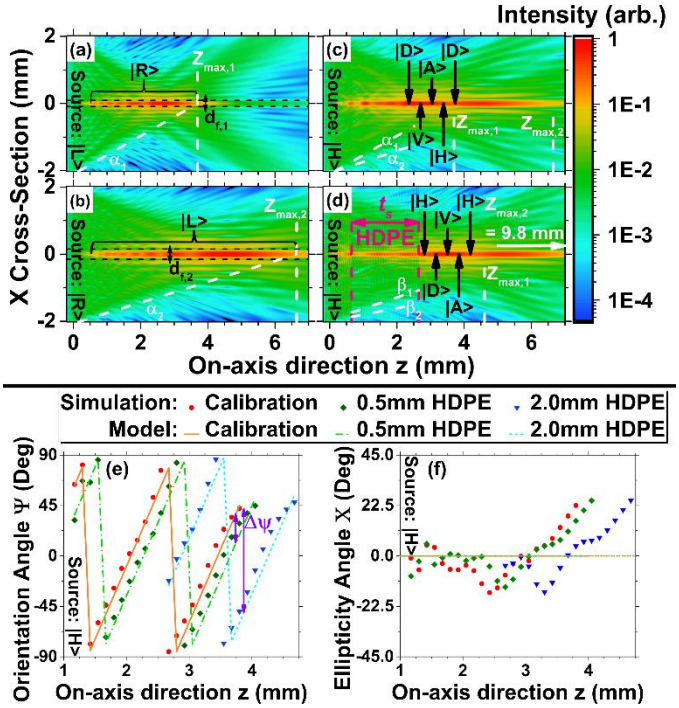

Fig. 3. Collective simulations of a metasurface with radius R_{MS} = 2 mm, g_1 = 0.24 mm and g_2 = 0.4 mm designed to independently generate two different Bessel beams for incident $|L\rangle$ and $|R\rangle$ polarized light (OPP). The axial x-z intensity profiles at y = 0 exhibits two independent Bessel beams, namely (a) B_1 for incident $|L\rangle$ and (b) B_2 for incident $|R\rangle$ polarized light. (c) Incident $|H\rangle$ light excites both Bessel beams, the superposition of which results in a linearly polarized beam center with rotating orientation angle $\Psi \propto z$ along the propagation direction (black arrows). (d) Inserting a homogeneous slab of dielectric material e.g., high-density polyethylene (HDPE, between pink dashed lines) into the beam path upon $|H\rangle$ excitation alters this superposition as a function of sample thickness t_s and refractive index n_s (2.0 mm and 1.58 RIU, respectively). Analysis of the (e) orientation angle $\psi(z)$ and (f) ellipticity angle $\chi(z)$ at the beam center (data points) provided a detailed analysis of the on-axis SoP with and without the HDPE slab in the beam path. The analytical model of (2)-(4) (lines) is in excellent agreement with the respective simulation results (data points).

Upon illuminating the same metasurface with $|H\rangle$ polarized light as shown in Fig. 3 (c), or any other linear SoP, one can observe a linearly polarized beam center the orientation angle ψ of which changes along the on-axis direction z. In this case, both constituent Bessel beams are excited simultaneously. All superimposed electric fields $E_{x1,2}$ and $E_{y1,2}$ along the focal line are constant and given by the chosen OPP. However, the on-axis phase shift $\delta_{1\leftrightarrow2}$ between rays of the two constituent Bessel beams B_1 and B_2 grows linearly with the propagation distance along z according to (2), with the spatial frequencies along the optical axis $k_{z1,2} = 2\pi\ /\ \lambda_0 \cdot cos\ (\alpha_{1,2})$.

$$\boldsymbol{\delta_{1\leftrightarrow2}(z) = z \cdot \left(\underbrace{k_{z1} - k_{z2}}_{:=\Delta k_z} \right)} \qquad \textbf{(2)}$$

This phase shift $\delta_{1\leftrightarrow2} \propto z$ translates into a linearly changing SoP along the focal line with a periodicity Λ_{SoP} given by (3).

$$\boldsymbol{\Lambda_{SoP} = 2\pi(\Delta k_z)^{-1} = \frac{\lambda_0}{cos\,\alpha_1 - cos\,\alpha_2}} \qquad \textbf{(3)}$$

The introduction of a homogeneous dielectric slab of sample thickness t_s and refractive index n_s into the beam path alters the internal half-cone angles $\beta_{1,2} = arcsin\left[sin(\alpha_{1,2})/n_s\right]$ according to Snell's law and the spatial frequencies according to $k_{n,z1,2}(n_s) = k_0 \cdot n_s \cdot cos\ (\beta_{1,2})$ for both beams, see Fig. 3 (d). The altered phase shift between B_1 and B_2 at any point on the optical axis z behind the slab is thus given by (4).

$$\boldsymbol{\delta_{1\leftrightarrow2}(z, t_s, n_s) = (z - t_s) \cdot (k_{z1} - k_{z2}) + t_s \cdot (k_{n,z1} - k_{n,z2})} \qquad \textbf{(4)}$$

In addition to a standing wave effect caused by Fabry-Perot resonances, Fig. 3 (d) clearly shows the decreased half-cone angles $\beta_{1,2}$ within a 2.0 mm thick slab of HDPE (n_{HDPE} = 1.58 RIU [15]) between the pink dashed lines. Both Bessel beams B_1 and B_2 were stretched in the axial direction within the sample since $\beta_{1,2} < \alpha_{1,2}$, resulting in an axial displacement of the transmitted rays after the sample region. This effect becomes more apparent when looking at the characteristic angles of the polarization ellipse, particularly the orientation angle $\Psi(z)$ in Fig. 3 (e). The observed change of Ψ along the optical axis without slab (red data points) is linear, with a simulated period Λ_{SoP} of 1.38 mm that is in excellent agreement with (3). For the same metasurface but behind the introduced HDPE samples of 0.5 mm (green diamonds) and 2.0 mm thickness (blue triangles), the previously mentioned axial displacement is observed as shift of the orientation angle $\Delta\Psi \propto t_s$ that is accurately described by our analytic model using (4). The on-axis ellipticity angle $\chi(z)$ of the SoP in Fig. 3 (f) remains close to the expected value of 0° until the shorter beam B_1 of Fig. 3 (a) becomes increasingly faint beyond ca. 3.5 mm.

The on-axis SoP along one axial period Λ_{SoP} is illustrated on the Poincare sphere in Fig. 4, from which one can infer the role of the metasurface's underlying OPP. For the metasurface design of Fig. 3 that responded to incident $|L\rangle$ and $|R\rangle$ light (black cubes), the on-axis SoP (red data points) circles around the equatorial S_1-S_2 plane with an axial frequency of z/Λ_{SoP}. However, a respective metasurface responding to incident $|D\rangle$ and $|A\rangle$ light follows a circular path along the meridial S_2-S_3 plane. In conclusion, our metasurface design provides control over the SoP formed along the focal line by choice of its underlying OPP (electric fields $E_{x1,2}$ and $E_{y1,2}$), whereas the oscillation length Λ_{SoP} can be chosen via the difference in radial phase periods $\Delta g = g_1 - g_2$ (opposite rotational sense for $g_1 > g_2$ and $g_1 < g_2$). The presented metasurface design enables various polarimetric applications in terahertz sensing and imaging by simply scanning the metasurface along the z-axis with respect to the object under study, as will be shown in the experimental results section.

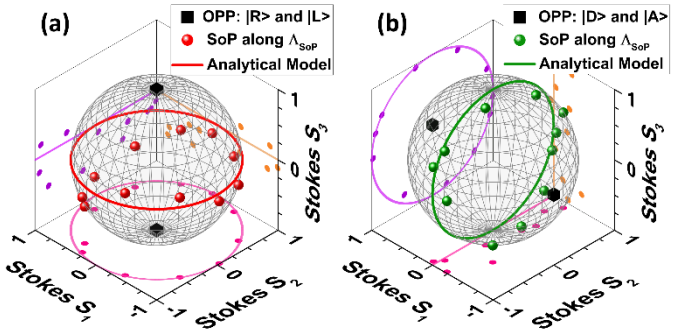

Fig. 4. Poincare sphere showing the SoP at the beam center (data points) for several equidistant positions (Δz = 125 µm) along a full axial SoP period Λ_{SoP} of 1.38 mm. Depicted are the simulation results for (a) the metasurface design with OPP responding to incident $|L\rangle$ and $|R\rangle$ polarised light (black cubes) employed in Fig. 3 and (b) an equivalent metasurface with OPP responding to incident $|D\rangle$ and $|A\rangle$ polarised light (black cubes).

B. Metasurface Fabrication and Evaluation

We developed a single-step photolithographic process to dry etch the metasurface layer into high resistivity silicon substrates (25 mm x 25 mm, 535 µm thick) using an ICP-DRIE Bosch method based on C_4F_8/SF_6 plasma chemistry [32]. A detailed description is given in supplement section S2.

Fig. 5 (a) shows a scanning electron micrograph of the pillar's sidewall profile exhibiting a close to vertical angle of 88.5°-89.5°. Fig. 5 (b) shows a plan view of a larger area of the metasurface. Optical interference profilometry (Bruker, ContourGT-X) was used to obtain a 3D profile of the pillars and their surrounding etch floor, as shown in Fig. 5 (c). A variation was observed in the etch depth owing to an effect known as aspect-ratio dependent etching (ARDE) [32]. The measured 3D data was analyzed as histogram over the depth dimension. The average etch depth $\bar{H} = \left(z_{pillar} - z_{floor}\right)$ is determined reliably with its standard deviation $\sigma_H = \sqrt{{\sigma_{pillar}}^2 + {\sigma_{floor}}^2}$ from a Gaussian fit to the histogram using the two peak positions z_{pillar} and z_{floor} and their respective variances ${\sigma_{pillar}}^2$ and ${\sigma_{floor}}^2$. The measured standard deviation of the etch depth σ_H was ±3.4 µm for the measurement data shown in Fig. 5 (c), or ±2.3 % of H.

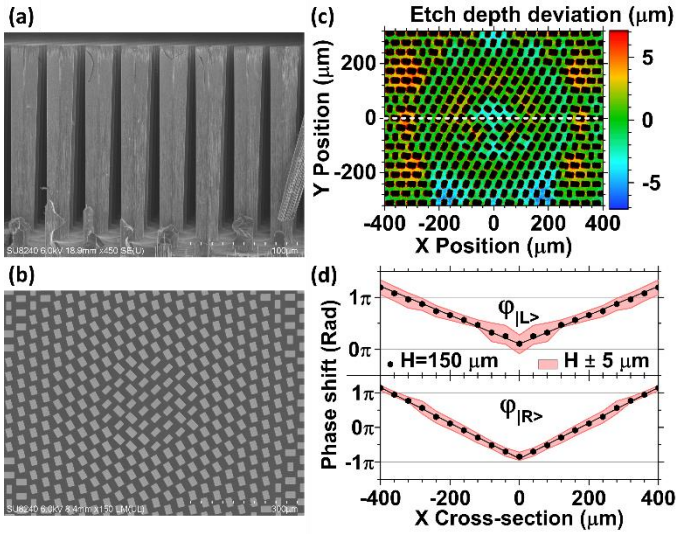

Fig. 5. Fabricated metasurface with pattern radius R_{MS} of 11 mm and radial phase periods $g_{|L\rangle}$ and $g_{|R\rangle}$ of 0.72 mm and 0.39 mm, which independently form |L⟩ and |R⟩ polarized Bessel beams when excited by light of opposite handedness, respectively. Scanning electron micrographs of (a) the pillar's sidewall profile for a cleaved metasurface and (b) the central region of the metasurface in plan view. (c) The 3D profile of the etch floor obtained with optical interference profilometry. Clusters of deviating etch depth (color scale) between the pillars (black) are apparent. (d) X cross-section of the encoded axicon phase profiles $\varphi_{|L\rangle}(x_i, 0)$, $\varphi_{|R\rangle}(x_i, 0)$ (black data points incl. linear fit) along the white dashed line shown in (c), including simulated phase deviations $\Delta\varphi_{|L\rangle,|R\rangle}$ for ± 5 µm ($\pm 1.5\ \sigma_H$) etch depth deviation (red bands).

Simulations of the pillars were rerun with adapted pillar height ΔH and substrate thickness of $\pm$ 5 µm ($\approx 1.5\ \sigma_H$) and $\pm$ 10 µm ($\approx 3\ \sigma_H$) to gauge the impact of the etch depth deviation on the device performance, as detailed in supplement section S3. All pillar geometries exhibited a linear relation ($R \geq 0.95$) between the resulting phase and height differences $\Delta\varphi_{x,y} \propto \Delta H$ [25] with a slope ranging from 2.1 °/µm to 6.7 °/µm, or on average (4.1 $\pm$ 1.0) °/µm. Fig. 5 (d) shows the central x cross-sections through the encoded axicon phase profiles $\varphi_{|L\rangle}$, $\varphi_{|R\rangle}$ along the white dashed line shown in Fig. 5 (c). For both $\varphi_{|L\rangle}$ and $\varphi_{|R\rangle}$, the phase shifts encoded by the individual pillars (black data points, H = 150 µm) accurately form the desired conical phase fronts (black lines). Taking a worst-case etch depth deviation of $\pm$ 5 µm - equal to 1.5 σ_H - into account resulted in the red error bands for the imposed phase profiles.

C. Experimental Setup for Polarimetric Imaging Microscopy

The experimental setup to use the beam forming metasurface for polarimetric imaging of the beam profile and NDT applications is shown in Fig. 6. An optically pumped continuous wave (cw) laser (FIRL 295, Edinburgh Instruments) delivered a collimated Gaussian beam (1/e radius ca. 5.5 mm) of up to 120 mW at 2.52 THz, which was $|H\rangle$ polarized. A non-polarizing beam splitter with power meter in its side arm was introduced to account for fluctuations of the output power between individual images. A pair of wire grid polarizers allowed for dynamic attenuation within the measurement arm by adjusting the angle of WGP 1 while leaving WGP 2 fixed to transmit $|H\rangle$. A custom-build telecentric objective that projected the 7.7x magnified detection plane z_{det} on to the camera's sensor (see supplement section S4) was placed behind the sample. A rotatable quarter wave plate (QWP), a fixed analyzer in |V⟩ transmission and a bandpass filter were integrated in the objective's infinity space. The combination of the QWP and fixed polarizer allows for measurement of the SoP [23]. The bandpass filter is used to increase the SNR at the terahertz camera (INO MicroXCam-384-THz).

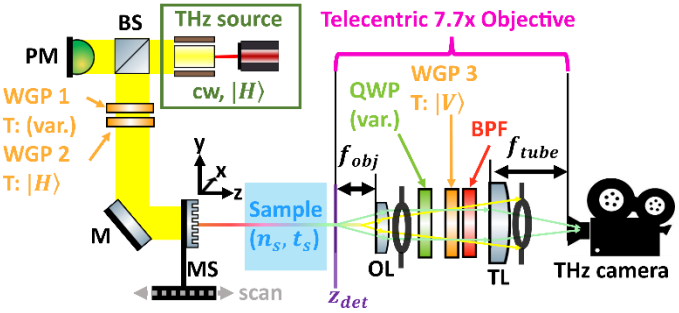

Fig. 6. Illustration of the experimental setup used for polarimetric beam profiling and sensing experiments at 2.52 THz in transmission geometry, including an optimized telecentric 7.7x objective (detailed in supplement section S4). BS: non-polarizing beam-splitter, PM: power meter, WGP: wire-grid polarizer, z_{det}: detection plane, QWP: Quarter wave plate, BPF: band pass filter, OL: objective lens, TL: tube lens.

III. Experimental Results

Fig. 7 shows experimental results obtained using the fabricated metasurface of Fig. 5 with pattern radius R_{MS} of 11 mm and radial phase periods $g_{|L\rangle}$ and $g_{|R\rangle}$ of 0.72 mm and 0.39 mm that generate |L⟩ and |R⟩ polarised Bessel beams, respectively. The half-cone angles $\alpha_{|L\rangle}$ and $\alpha_{|R\rangle}$ were predicted to be 9.5º and 17.8º, creating a theoretical oscillation period of the on-axis SoP Λ_{theo} of 3.45 mm using (3).

The transverse polarization profile can be generated pixel-by-pixel from eight individual images with incrementally rotated QWP by 22.5° using the setup of Fig. 6, see supplement section S5 for a detailed description. Such polarization-resolved images of the probe beam are shown in Fig. 7 (a) and (b), depicting the characteristic angles $\Psi(x, y)$ and $\chi(x, y)$ of each pixel's polarization ellipse, respectively. The transverse profiles of both 0th order Bessel beams form equidistant concentric rings around the beam center in Fig. 7 (a) and (b), with the white and black dotted circles representing $d_{f,|L\rangle}$ and $d_{f,|R\rangle}$, respectively. The beam center exhibited uniform Ψ and χ close to 0°, corresponding to $|H\rangle$ light. The circular mean of

the pixel values within the beam center (diameter of $2/3 \cdot d_{f,|R\rangle}$) was calculated as reliable and reproducible SoP for each respective scan position z_i along the focal line. The residual $|L\rangle$ and $|R\rangle$ components in Fig. 7 (b) are a result of the steeper half-cone angle $\alpha_{|R\rangle} > \alpha_{|L\rangle}$, creating a more tightly focused beam center $d_{f,|R\rangle} < d_{f,|L\rangle}$ for the $|R\rangle$ wavefront. The more tightly focused beam center for $|R\rangle$ caused a slightly imbalanced superposition ($I_{|R\rangle} > I_{|L\rangle}$) of the two constituent Bessel beams $B_{|R\rangle}$ and $B_{|L\rangle}$ with some residual ellipticity at the beam center ($I_{res} = I_{|R\rangle} - I_{|L\rangle}$) and the radially alternating rings of predominantly $|L\rangle$ or $|R\rangle$ components seen in Fig. 7 (b). The residual center ellipticity χ can be exploited to assess the quality of polarimetric images since it provides information on potential misalignments between the constituent beams $B_{|R\rangle}$ and $B_{|L\rangle}$, and whether the maximum scan range $z_{max}(B_{|R\rangle})$ of the shorter beam has been surpassed ($I_{|R\rangle} \ll I_{|L\rangle}$).

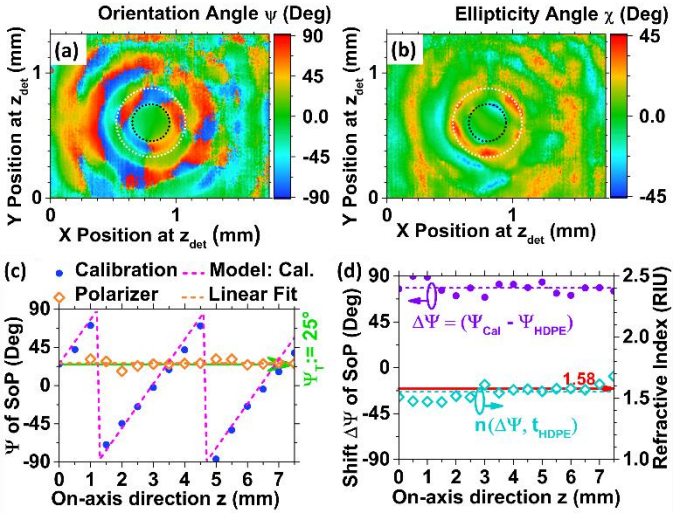

Fig. 7. Results of beam profiling and sensing experiments employing the fabricated metasurface of Fig. 5 within the setup outlined in Fig. 6. The transversal profiles of (a) the orientation angle $\Psi(x,y)$ and (b) the ellipticity angle $\chi(x,y)$ of each pixel's polarization ellipse. The white and black dotted circles represent the central lobes of both Bessel beams with diameter $d_{f,|L\rangle}$ and $d_{f,|R\rangle}$, respectively. (c) Comparison between the axial orientation angle $\Psi(z)$ without sample (blue data points) and with linear polarizer ($\psi_T = 25°$, green line) in the beam path, showing the ability to correctly determine the transmission axis of diattenuating media (orange diamonds, $\bar{\psi}$ = 26.2° ± 3.7°). (d) Refractive index measurement of a 5.65 mm thick HDPE sample inside the beam path (violet data points). The measured sample thickness and averaged shift $\Delta\Psi$ = 78.3° ±6.0° of the orientation angle relative to the previous calibration served as input for our analytic model of (4) to determine a refractive index of 1.55 ± 0.06 RIU (n_{Lit}(HDPE) = 1.58 RIU [15]).

In contrast, the SoP's orientation angle Ψ is exclusively defined by the superposition of equal circular components ($I_{|L\rangle} \equiv I_{|R\rangle}$) and their phase difference $\delta_{|L\rangle \leftrightarrow |R\rangle}$. Ψ is thus robust against perturbations caused by intensity variations in I_{res} or misalignment and is therefore well suited to be a measurement channel in the following sensing experiments. Fig. 7 (c) shows the progression of the SoP's orientation angle ψ along the focal line obtained in a calibration scan (blue data points). The observed linear course is in excellent quantitative agreement with our model of (3), (4) (dashed magenta line) with Λ_{exp} of 3.57 mm very close to its theoretical value of 3.45 mm. The setup's capability to analyze a sample's diattenuation was tested using a randomly oriented wire grid polarizer. The axial SoP beating observed in the calibration measurement changed into a sine-shaped on-axis intensity beating with $\psi(z) \approx$ const. (orange diamonds) after the polarizer was introduced into the beam. The known orientation of the polarizer's transmission axis of ψ_T = 25° (green line) was measured to be 26.2° ± 3.7° by averaging all scan positions (orange dashed line).

Finally, Fig. 7 (d) demonstrates the ability to measure the refractive index n_{HDPE} of a sample of known thickness (t_{HDPE} = 5.65 mm). The on-axis orientation angle $\Psi(z)$ at the beam center exhibits a shift $\Delta\Psi = \left(\Psi_{Cal}(z) - \Psi_{HDPE}(z)\right)$ averaged to 78.3° ± 6.0° (violet data points) after transmission through a the HDPE sample compared to the calibration, as expected from the simulations shown in Fig. 3 (e) and the analytical model of (2)-(4). This SoP shift $\Delta\Psi(z) \approx$ const. was used together with the known sample thickness t_{HDPE} to retrieve the measured refractive index (cyan data points) using the analytical model. The measured refractive index of 1.55 RIU ± 0.06 RIU was obtained by averaging over all data points of this graph and is close to the literature value of 1.58 RIU (red line) [15]. Note that the measurement sensitivity $S_{RI} = \Delta\Psi/(t_s \cdot [n_s - 1])$ (the SoP change in response to change in optical path length) is set by the metasurface design parameters. Increasing $\Delta g = g_1 - g_2$ will increase $\alpha_{1,2}$ and $\beta_{1,2}(n_s)$ hence $\delta_{1\leftrightarrow 2}(z, t_s, n_s)$ and thus the measured signal $\Delta\Psi$. The dynamic measurement range $\Delta n_{max} = [\pi / (S_{RI} \cdot t_s)] - 1$ will decrease as a trade-off, limiting the range within which refractive indices exhibit an unambiguous shift $\Delta\Psi \leq \pi$. The measurement sensitivity S_{RI} of the metasurface employed in Fig. 7 was 23.9 °/mm·RIU (or 417.1 m^{-1}) with a dynamic range Δn_{max} of 2.62 RIU for t_{HDPE} = 5.65 mm.

IV. Conclusion

We have presented an innovative concept for a terahertz beam forming metasurface that exploits the state of polarization as an information channel. The versatile metasurface design is capable of controlling the transmitted phase- and polarization-front using anisotropic dielectric pillars to form a probe beam. The component was monolithically fabricated by etching into high resistivity (> 10 kΩcm) silicon to yield an experimental transmission efficiency of up to 76.0 ± 0.4 %. Detailed evaluation of the fabrication tolerances demonstrated a practically insignificant degradation of the metasurface's optical performance. The result is a single compact optic that minimizes the refraction and diffraction problems associated with constructing a multi-component system [21, 27-29].

An analytical model was developed to predict the axial progression of the SoP of the resulting probe beam from its

constituent pair of orthogonally polarized Bessel beams. The model was shown to be in good agreement with detailed simulations and experimental data.

The metasurface was embedded as a beam forming condenser lens in a polarimetric imaging microscope and both the probe beam's transverse profile and on-axis change of the SoP were found to closely match theoretical predictions. The microscope was used in sensing applications including the measurement of the diattenuation and refractive index of a homogeneous sample. The resulting instrument for refractive index sensing is the first of its kind to operate at terahertz wavelengths and showed improved measurement sensitivity and dynamic range when compared to previous work at a wavelength of 532 nm [21]. Compared to established techniques such as terahertz time-domain spectroscopy (THz-TDS), our approach can provide rich polarimetric information on the sample e.g., diattenuation and birefringence. Respective polarimetric measurements using THz-TDS typically require two measurements with rotated sample by 90º, thereby only analyzing two orthogonal linear SoPs rather than the complete polarisation ellipse. Furthermore, our approach allows for the use of large pixel arrays to image a wide field-of view (FOV), whereas THz-TDS imaging typically requires slow lateral pixel-by-pixel scanning of the sample. The image acquisition time of the presented setup is limited by the slow SoP measurement (rotating QWP method [23]) that can be accelerated to as little as 1.2 s when combined with a previously published metasurface polarimeter [20]. In terms of data processing, we expect our technique to be easily automated and compare favorably with THz-TDS with respect to data volume and processing when considering images of similar FOV since 8 intensity measurements per pixel are processed for our technique compared to the temporal information of each pixel in THz-TDS. THz-TDS has the advantage of providing spectral sample information. Although our demonstrator setup used a monochromatic light source, we expect from previous studies that the type of metasurface presented here should maintain good operation over a bandwidth of more than 1 THz [20]. Consequently, the presented metasurface design could also be used as an optic in a THz-TDS system with the potential to add further functionality to existing instruments.

Future work should explore further optimization and extension of both beam forming and setup capabilities to enable polarimetric imaging of heterogeneous samples. Furthermore, a new imaging instrument is envisioned that would be capable of analyzing the reflection from a sample with the incident probe beam. Such a setup could retrieve a 3D surface profile from polarimetric information and the diattenuating or birefringent behavior of the sample simultaneously. Such an instrument could in future have a role in non-destructive testing of polymers and resin-based composites.

ACKNOWLEDGMENT

The authors thank the staff of the James Watt Nanofabrication Centre for their support in device fabrication and maintaining the infrastructure that was crucial to this publication. Special thanks go to Corrie Farmer for his relentless efforts in developing and optimizing fabrication and dry etch recipes on a world-class level.

REFERENCES

[1] S. S. Dhillon *et al.*, "The 2017 terahertz science and technology roadmap," *Journal of Physics D: Applied Physics*, vol. 50, no. 4, 2017, doi: 10.1088/1361-6463/50/4/043001.

[2] H. Guerboukha, K. Nallappan, and M. Skorobogatiy, "Toward real-time terahertz imaging," *Advances in Optics and Photonics*, vol. 10, no. 4, 2018, doi: 10.1364/aop.10.000843.

[3] G. Valusis, A. Lisauskas, H. Yuan, W. Knap, and H. G. Roskos, "Roadmap of Terahertz Imaging 2021," *Sensors (Basel)*, vol. 21, no. 12, Jun 14 2021, doi: 10.3390/s21124092.

[4] Y. Cheng, Y. Wang, Y. Niu, and Z. Zhao, "Concealed object enhancement using multi-polarization information for passive millimeter and terahertz wave security screening," *Opt Express*, vol. 28, no. 5, pp. 6350-6366, Mar 2 2020, doi: 10.1364/OE.384029.

[5] H. Feng *et al.*, "A passive video-rate terahertz human body imager with real-time calibration for security applications," *Applied Physics B*, vol. 126, no. 8, 2020, doi: 10.1007/s00340-020-07496-3.

[6] M. Kato, S. R. Tripathi, K. Murate, K. Imayama, and K. Kawase, "Non-destructive drug inspection in covering materials using a terahertz spectral imaging system with injection-seeded terahertz parametric generation and detection," *Opt Express*, vol. 24, no. 6, pp. 6425-32, Mar 21 2016, doi: 10.1364/OE.24.006425.

[7] Y. Peng, C. Shi, Y. Zhu, M. Gu, and S. Zhuang, "Terahertz spectroscopy in biomedical field: a review on signal-to-noise ratio improvement," *PhotoniX*, vol. 1, no. 1, 2020, doi: 10.1186/s43074-020-00011-z.

[8] A. I. Nikitkina *et al.*, "Terahertz radiation and the skin: a review," *J Biomed Opt*, vol. 26, no. 4, Feb 2021, doi: 10.1117/1.JBO.26.4.043005.

[9] C. Kulesa, "Terahertz Spectroscopy for Astronomy: From Comets to Cosmology," *IEEE Transactions on Terahertz Science and Technology*, vol. 1, no. 1, pp. 232-240, 2011, doi: 10.1109/tthz.2011.2159648.

[10] D.-H. Han and L.-H. Kang, "Nondestructive evaluation of GFRP composite including multi-delamination using THz spectroscopy and imaging," *Composite Structures*, vol. 185, pp. 161-175, 2018, doi: 10.1016/j.compstruct.2017.11.012.

[11] J. Dong *et al.*, "Visualization of subsurface damage in woven carbon fiber-reinforced composites using polarization-sensitive terahertz imaging," *NDT & E International*, vol. 99, pp. 72-79, 2018, doi: 10.1016/j.ndteint.2018.07.001.

[12] J. Dong, B. Kim, A. Locquet, P. McKeon, N. Declercq, and D. S. Citrin, "Nondestructive evaluation of forced delamination in glass fiber-reinforced composites by terahertz and ultrasonic waves," *Composites Part B: Engineering*, vol. 79, pp. 667-675, 2015, doi: 10.1016/j.compositesb.2015.05.028.

[13] K. Sengupta, T. Nagatsuma, and D. M. Mittleman, "Terahertz integrated electronic and hybrid electronic–photonic systems," *Nature Electronics*, vol. 1, no. 12, pp. 622-635, 2018, doi: 10.1038/s41928-018-0173-2.

[14] V. S. Philipp Kuehne, Nerijus Armakavicius, Mathias Schubert, and Vanya Darakchieva, "Stealth technology-based Terahertz frequency-domain ellipsometry instrumentation," *IEEE Transactions on Terahertz Science and Technology*, 2017, doi: 10.48550/arXiv.1712.05283.

[15] P. D. Cunningham *et al.*, "Broadband terahertz characterization of the refractive index and absorption of some important polymeric and organic electro-optic materials," *Journal of Applied Physics*, vol. 109, no. 4, pp. 043505-043505-5, 2011, doi: 10.1063/1.3549120.

[16] J. P. Balthasar Mueller, N. A. Rubin, R. C. Devlin, B. Groever, and F. Capasso, "Metasurface Polarization Optics: Independent Phase Control of Arbitrary Orthogonal States of Polarization," *Phys Rev Lett*, vol. 118, no. 11, p. 113901, Mar 17 2017, doi: 10.1103/PhysRevLett.118.113901.

[17] A. Arbabi, Y. Horie, M. Bagheri, and A. Faraon, "Dielectric metasurfaces for complete control of phase and polarization with subwavelength spatial resolution and high transmission," *Nat Nanotechnol*, vol. 10, no. 11, pp. 937-43, Nov 2015, doi: 10.1038/nnano.2015.186.

[18] N. A. Rubin, G. D'Aversa, P. Chevalier, Z. Shi, W. T. Chen, and F. Capasso, "Matrix Fourier optics enables a compact full-Stokes polarization camera," *Science*, vol. 365, no. 6448, Jul 5 2019, doi: 10.1126/science.aax1839.

[19] A. H. Dorrah, N. A. Rubin, A. Zaidi, M. Tamagnone, and F. Capasso, "Metasurface optics for on-demand polarization transformations along the

optical path," *Nature Photonics*, vol. 15, no. 4, pp. 287-296, 2021, doi: 10.1038/s41566-020-00750-2.

[20] T. S. Nowack *et al.*, "Terahertz polarimetry with a monolithic metasurface," *Optics Letters*, vol. 47, no. 16, 2022, doi: 10.1364/ol.463143.

[21] A. H. Dorrah, M. Zamboni-Rached, and M. Mojahedi, "Experimental demonstration of tunable refractometer based on orbital angular momentum of longitudinally structured light," *Light Sci Appl*, vol. 7, p. 40, 2018, doi: 10.1038/s41377-018-0034-9.

[22] R. C. Devlin, A. Ambrosio, N. A. Rubin, J. P. B. Mueller, and F. Capasso, "Arbitrary spin-to-orbital angular momentum conversion of light," *Science*, vol. 358, no. 6365, pp. 896-901, Nov 17 2017, doi: 10.1126/science.aao5392.

[23] B. Schaefer, E. Collett, R. Smyth, D. Barrett, and B. Fraher, "Measuring the Stokes polarization parameters," (in English), *American Journal of Physics*, vol. 75, no. 2, pp. 163-168, Feb 2007, doi: 10.1119/1.2386162.

[24] R. Appleby, T. D. Drysdale, J. M. Chamberlain, D. R. S. Cumming, and K. A. Krapels, "A micromechanical beam-steering device for terahertz systems," presented at the Passive Millimetre-Wave and Terahertz Imaging and Technology, 2004.

[25] M. Khorasaninejad *et al.*, "Polarization-Insensitive Metalenses at Visible Wavelengths," *Nano Lett*, vol. 16, no. 11, pp. 7229-7234, Nov 9 2016, doi: 10.1021/acs.nanolett.6b03626.

[26] X. Zang *et al.*, "Polarization-Insensitive Metalens with Extended Focal Depth and Longitudinal High-Tolerance Imaging," *Advanced Optical Materials*, vol. 8, no. 2, 2019, doi: 10.1002/adom.201901342.

[27] I. Moreno, J. A. Davis, M. M. Sanchez-Lopez, K. Badham, and D. M. Cottrell, "Nondiffracting Bessel beams with polarization state that varies with propagation distance," *Opt Lett*, vol. 40, no. 23, pp. 5451-4, Dec 1 2015, doi: 10.1364/OL.40.005451.

[28] S. Fu, S. Zhang, and C. Gao, "Bessel beams with spatial oscillating polarization," *Sci Rep*, vol. 6, p. 30765, Aug 4 2016, doi: 10.1038/srep30765.

[29] P. Li *et al.*, "Generation and self-healing of vector Bessel-Gauss beams with variant state of polarizations upon propagation," *Opt Express*, vol. 25, no. 5, pp. 5821-5831, Mar 6 2017, doi: 10.1364/OE.25.005821.

[30] D. McGloin and K. Dholakia, "Bessel beams: Diffraction in a new light," *Contemporary Physics*, vol. 46, no. 1, pp. 15-28, 2005, doi: 10.1080/0010751042000275259.

[31] S. Ding, Q. Li, R. Yao, and Q. Wang, "Brewster's angle method for absorption coefficient measurement of high-resistivity silicon based on CW THz laser," *Applied Physics B*, vol. 98, no. 1, pp. 119-124, 2009, doi: 10.1007/s00340-009-3611-z.

[32] H. V. Jansen, M. J. de Boer, S. Unnikrishnan, M. C. Louwerse, and M. C. Elwenspoek, "Black silicon method: X. A review on high speed and selective plasma etching of silicon with profile control: an in-depth comparison between Bosch and cryostat DRIE processes as a roadmap to next generation equipment," *Journal of Micromechanics and Microengineering*, vol. 19, no. 3, 2009, doi: 10.1088/0960-1317/19/3/033001.

Thomas S. Nowack received his B.Sc. in functional materials from the University of Würzburg and his M.Sc. in organic & molecular electronics from Dresden University of Technology. He was recently awarded his PhD from the University of Glasgow and was Early-Stage Researcher of the EU's MSCA-ITN 'TeraApps'.
His current research focusses on the development of compact and efficient metasurface optics operating at terahertz frequencies to test novel imaging and sensing concepts i.e., by utilizing tailored polarization effects.

Yash D. Shah received the B.E. (Hons.) degree from Mumbai University, India, the M.S. degree from Northwestern University, USA, where he focused on 2DEG low temperature measurements with capacitive contacts, and the Ph.D. degree from the University of Cambridge, U.K., working on THz quantum cascade lasers design and fabrication. He was a PDRA for 5 years at the University of Glasgow, U.K., where his expertise lay in nanophotonics, metasurfaces and quantum optics. Having left academia, he co-founded Metahelios Ltd where he is the director and CTO.

James Grant received the B.Sc. and Ph.D. in physics from the University of Glasgow in 2002 and 2006 respectively. Between 2007 and 2019 he was a postdoctoral researcher within the School of Engineering at the University of Glasgow where his research interests included nanofabrication, metamaterial devices, plasmonics, terahertz systems, sensors and imaging and CMOS electronics.
He is currently a Research Engineer in Plasma Processing in the James Watt Nanofabrication Centre at the University of Glasgow.

Ivonne Escorcia Carranza received the B.E. degree in electrical engineering from John Brown University, AR, USA, in 2007, the M.S.E.E degree from the University of Arkansas, Fayetteville, USA, in 2010, and Ph.D. degree in electronics and electrical engineering from the University of Glasgow, Scotland, UK, in 2015 where she worked with the Microsystem Technology group.
She currently works as an Electronics Engineer in the defense sector. Her research interests include analog and mixed-signal IC design, image sensors, and terahertz imaging. She is a member of Eta Kappa Nu society.

Mitchell Kenney (MSci, PhD) is a Nottingham Research Fellowship holder at the University of Nottingham, and leader of the ultrathin optics and metasurfaces research group since 2020. He received both his MSci and PhD in nanotechnology and metamaterials at the University of Birmingham, prior to joining the University of Glasgow as postdoctoral researcher and proleptic lecturer.
His current research focusses on visible metamaterial lenses for three-dimensional microscopy and imaging applications, combining computational imaging techniques with novel metamaterial design principles. He is co-lead of the EPSRC-funded UK Metamaterials Network *Photonic Metamaterials* group.

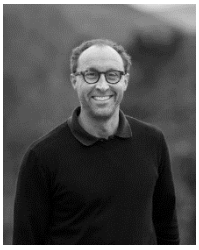

Daniele Faccio obtained a degree in physics from the University of Milano, Italy in 1997 and a PhD from the University of Nice Sophia-Antipolis, France in 2007. His main field of study is classical optics and quantum photonics, with an interest in fundamental quantum physics and applications in healthcare.
He was assistant professor at the University of Insubria, Italy (2004-2010), Associate professor (2010-2012) and then full professor (2012-2018) at Heriot-Watt University.
He is currently professor in quantum technologies at the University of Glasgow.

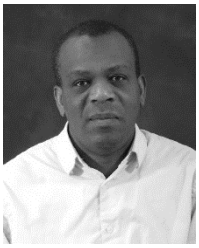

Edward Wasige (Senior Member, IEEE) received the BSc. (Eng.) degree in Electrical Engineering from the University of Nairobi, Kenya, in 1988, the MSc.(Eng.) from the University of Liverpool (UK) in 1990, and the PhD degree in Electrical Engineering from Kassel University (Germany) in 1999. Prior to joining the University of Glasgow in 2002, he was a UNESCO postdoctoral fellow at the Technion – Israel Institute of Technology. He is Professor and leads the High Frequency Electronics research group with focus on gallium nitride transistor technologies and on terahertz electronics based on resonant tunnelling diode technologies.

David R. S. Cumming (IEEE Fellow, BEng, PhD) is the Professor of Electronic Systems at the University of Glasgow. He has worked as a VLSI design engineer with STMicroelectronics, post-doctoral researcher at Glasgow University and as a lecturer at the University of Canterbury, NZ. Since 1999 he has been at Glasgow University. He has published over 300 papers on sensor and photonic technologies. He is FRSE, FREng and FIEEE.